Optimizing The X-ray Optics Fabrication Process for BabyIAXO
REU Program at Columbia University - Nevis Labs

Vyshu Sabbi[1]

[1]University of North Carolina-Chapel Hill

August 15, 2025

Abstract

Theoretical axions have caught the attention and imagination of physicists all over the globe. Predicted by the Peccei-Quinn theory, axions offer a compelling solution to both the Strong CP problem and the mysterious dark matter. As an extension of the Standard Model of Particle Physics, these light, loosely interacting particles could be produced in stellar cores through the Primakoff effect, which results from axion-photon coupling. The International Axion X-ray Observatory (IAXO) is the next generation axion helioscope designed to detect axions potentially generated in the Sun's core with novel sensitivity through the use of an x-ray optic to increase the signal-to-noise ratio. This summer's work focuses on optimizing several key components of the optic fabrication process: thermal glass slumping technique, laser scanning characterization, and glass cutting into conic sections. This work aims to standardize and streamline the production of 103 optical layers, focusing on 120mm diameter layers to improve reproducibility and efficiency of the optic fabrication.

Contents

1 Background

1.1 Strong CP Problem and Peccei-Quinn Theory

The strong C-P problem emerged as one of the biggest unresolved problems in particle physics since the late 1970s. CP stands for charge conjugation-parity symmetry. Charge conjugation is a transformation when a particle is replaced with its antiparticle, usually in the form of flipping its charge, while parity is a transformation in which the spatial coordinates are replaced with its mirror (e.g. $x = 5 \rightarrow x = -5$). CP Symmetry states that the laws of physics should be the same if charge conjugation and parity transformations are acted on a system. The Standard Model predicts that CP symmetry should be conserved for the electromagnetic force, but can be broken for both the weak and strong forces. The problem arises experimentally. This Standard Model prediction holds true for the weak force, but has been experimentally violated for the strong force. This is because we haven't observed CP violation in the strong force up to high precision [2].

A well known example of this mysterious CP conservation is the neutron electric dipole moment (EDM). The neutron is made of quarks, which theoretically could be arranged in any way, as shown in Fig. 1 on the left. The θ is the CP violating parameter for the strong force. The Standard Model tells us that this parameter can be nonzero as shown, so we expect the neutron to have an electric dipole moment. Yet without known reason, it has remained experimentally unobserved to about 10^{-26} precision, which is effectively zero [1]. The effort to explain small parameters has proven useful in the past to gain a deeper understanding of nature. The strong CP problem could therefore give us a unique way to search for new physics.

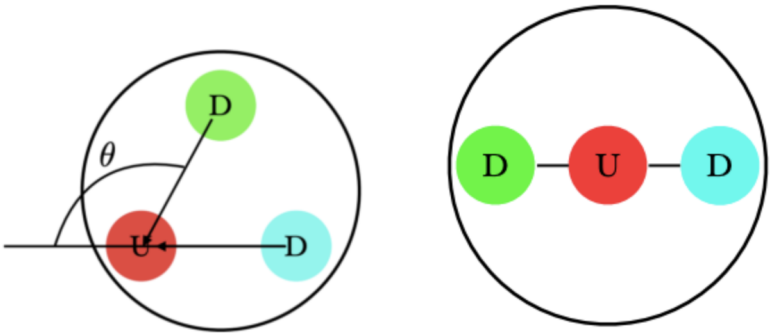

Figure 1: Left: *Expected neutron EDM. Each colored circle is a quark, with 'U' denoting the up quark and 'D' denoting the down quark. The θ is the CP violating parameter for the strong force.* ***Right:*** *What the neutron looks like experimentally. Here, $\theta \approx 0$ and the charges of the quarks cancel each other out, making the neutron EDM effectively zero [6].*

In 1977, Roberto Peccei and Helen Quinn proposed a way to fix this problem via adding a new dynamic field that would naturally cancel out the standard model CP violating θ term shown in Fig. 1. They introduced a new symmetry called the Peccei-Quinn (PQ) symmetry. This theory predicts a particle, known as the axion, to emerge when this symmetry is spontaneously broken. The axion, also known as the QCD (quantum chromodynamics) axion, is an electrically neutral, spinless particle with at most small

coupling with the known standard model particles like photons (mediators of the electromagnetic force) or gluons (mediators of the strong force). This specific theory has gained a lot of traction because QCD axions are both the only known testable solution to the CP problem and well-motivated dark matter candidates [2].

1.2 Axions

1.2.1 QCD Axions and ALPs

While the following discussion is not directly tied to the experimental results presented, it offers a theoretical perspective that motivates the science behind the BabyIAXO helioscope.

The QCD axion is the hypothetical particle that arises from the Peccei–Quinn theory and has several key properties, such as their coupling to gluons. This axion-gluon coupling is essential, as it allows the axion to cancel out CP violation in QCD by effectively shifting, or "rotating," the CP-violating θ term from Fig. 1 to zero. The axion field modifies the θ parameter into an effective $\theta(\theta_{eff})$. A nonzero axion field generates an axion potential that is minimized when the $\theta_{eff} \approx 0$. This dynamically solves the strong CP problem.

This rotational symmetry is a characteristic of the U(1) group, a mathematical group consisting of all 1×1 unitary matrices. In other words, U(1) is a group of all complex numbers with magnitude 1, such as $e^{i\theta}$. This group geometrically corresponds to a circle, where multiplying elements in this group together is equivalent to adding the θ parameter ($e^{i\theta_1} \times e^{i\theta_2} = e^{i(\theta_1+\theta_2)}$). Rotating by the resulting theta around the circle is symmetric; this is known as a U(1) symmetry. QCD axions arise from the spontaneous breaking of the Peccei–Quinn (PQ) symmetry, a global U(1) symmetry, to dynamically relax the CP violating θ term to zero [2]. This means the axion field shift would equal the CP-violating θ term, canceling out θ and conserving CP symmetry in the strong force.

Axions can interact with both gluons and photons, which happen from anomalous breaking of the PQ symmetry under QCD and QED (quantum electrodynamics). This means that while the PQ symmetry is conserved at the classical (global) level, quantum effects (via anomalies) introduce PQ symmetry violations that allow the axion to interact with gauge fields like gluons and photons; interactions that are important for both axion theory and axion experimental detection strategies [2]. These quantum anomalies set the strength of the axion coupling to gluons and photons. Due to this QCD anomaly and its U(1) symmetry breaking origin, the QCD axion is classified as a pseudo-Nambu-Goldstone boson, which means it has a naturally light and feebly interacting nature [2]

QCD axions fall into a broader class of theorized particles known as axion-like particles (ALPs). ALPs have similar properties to axions and arise naturally through many extensions of the Standard Model like string theory [2]. Unlike QCD axions, ALPs don't couple to gluons, thus are not a viable candidate to solve the Strong CP Problem. Though, both QCD axions and ALPs are strong dark matter candidates, so ALPs are still a focus of many particle physics experiments.

1.2.2 The Primakoff Effect: Generating Axions Through Axion-Photon Coupling

All axion-like particles (ALPs), including QCD axions, couple to photons. The Primakoff effect, shown in Fig. 2, is a theorized process where a real photon interacts with a virtual photon in the presence of a strong magnetic field to convert into an axion.

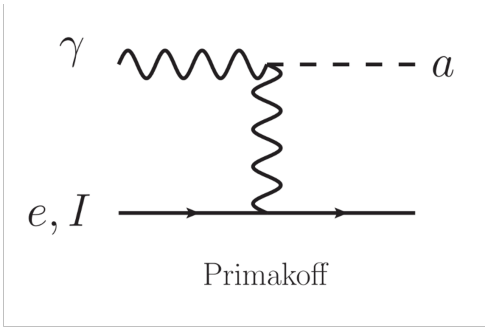

Figure 2: *Feynmann diagram for the Primakoff Effect [11].*

This effect is particularly important because in order for a particle to fall into the ALP category, it must couple to photons, making the Primakoff interaction one of the most generic method to search for ALPs. This effect also provides an experimentally powerful way to detect them given the amount of photons in a strong magnetic field we have access to from the sun and our current technological capabilities to build experiments sensitive to the axions produced via the Primakoff effect.

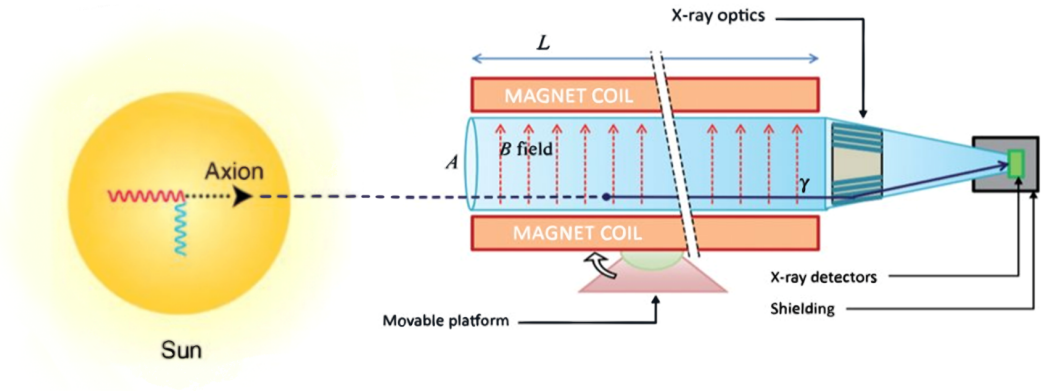

Figure 3: *Axion helioscope concept. [12].*

Fig. 3 shows a diagram of an axion helioscope, an experimental way to detect axions via the Primakoff effect. In the Sun's core, the real photon originates from blackbody radiation, which peaks in the X-ray range, and the virtual photons are supplied by the solar core's electromagnetic field. When a blackbody X-ray photon from the solar core interacts with a virtual photon, it may convert into an axion. These axions, due to their feeble interaction with Standard Model particles, are able to escape the solar core, a small

portion of which travel to Earth and enter the axion helioscope. The ideal environment to cause the reverse Primkoff conversion can be created in the laboratory to reconvert solar axions back into X-ray photons.

However, this interaction is incredibly rare. Converting these solar axions back into a signal to detect with confidence requires a strong magnet and low background.

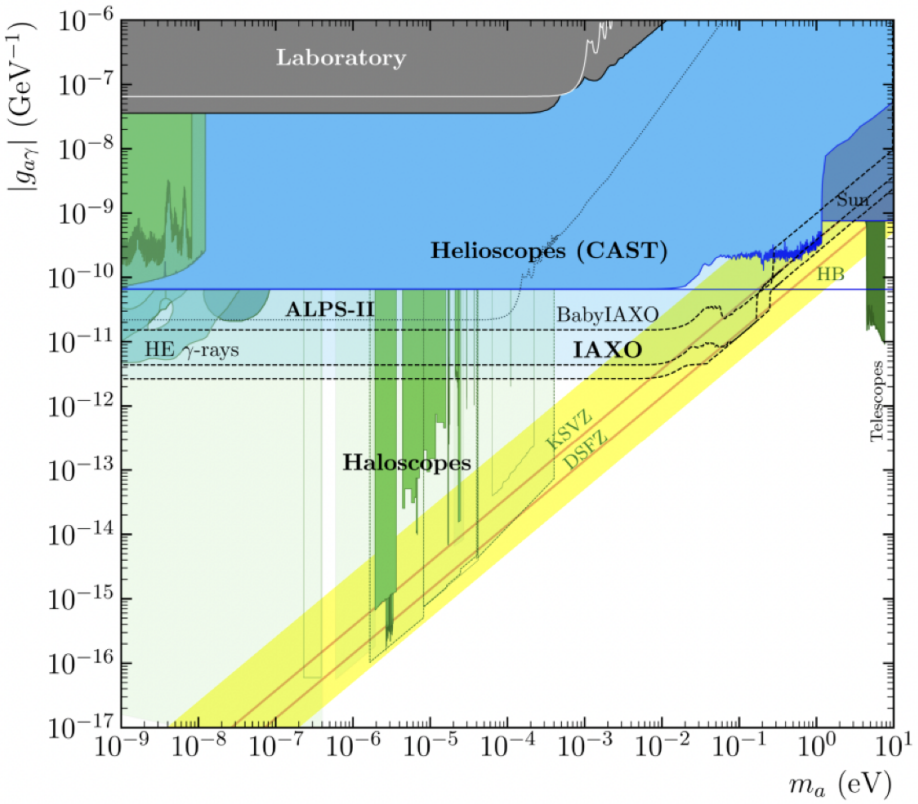

Figure 4: *Axion-photon coupling parameter space plot; axion-photon coupling constant vs. axion mass. Solid colors: different experiments that have made progress in this parameter space. Translucent colors: targeted progress of proposed experiments. Yellow band: QCD axion parameter space. Within this band are the leading QCD axion theories, Kim–Shifman–Vainshtein–Zakharov (KSVZ) and Dine–Fischler–Srednicki–Zhitnisky (DFSZ) [4].*

Fig. 4 illustrates the investigation of the parameter space for axion-photon coupling by plotting axion-photon coupling constant against axion mass. Different experiments that have explored this parameter space are indicated by various solid colors. The QCD axion-photon coupling parameter space is shown by the yellow band, which has a strictly calculated relationship between axion-photon coupling constant and axion mass. Higher values on the y-axis signify stronger axion-photon coupling, making experimental detection easier due to a stronger signal, while lower values necessitate more sensitive experiments. Higher values on the x-axis means heavier axion mass which indicates particle-like behavior, while lighter masses suggest wave-like behavior. The particle-like vs. wave-like behavior determines the experimental techniques employed for axion detection. The two main experiment types are haloscopes, which are optimized for specific lower mass ranges and mainly search for axion-like particles (ALPs) through galactic halos, and helioscopes, which probe broad mass ranges and are focus on solar axions [2].

The CERN Axion Solar Telescope (CAST) is the previous generation helioscope that cleared out much of the parameter space up till more than 10^{-10} coupling (solid blue region in Fig. 4). Note that the sensitivity of CAST did not probe the QCD axion coupling range (yellow band in Fig. 4).

1.3 International Axion Observatory

The International Axion Observatory (IAXO) is the next generation axion helioscope searching for solar axions, and is the only experiment designed to probe the QCD axion mass range on the heavier end (greater than 10^{-3} eV). BabyIAXO, currently under development, serves as the prototype for IAXO to demonstrate all the major technologies [4].

Even BabyIAXO has discovery potential by exploring unknown territory down to almost 10^{-11} coupling, pushing the previous coupling limit by around 1 order of magnitude (Fig. 4).

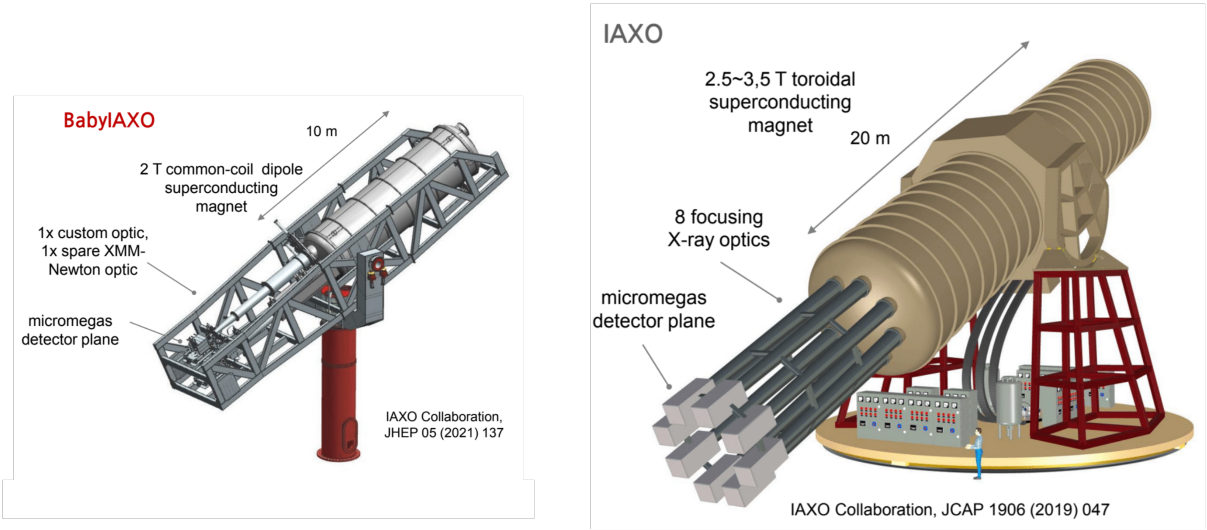

Figure 5: Left: *Diagram of BabyIAXO.* ***Right:*** *Diagram of IAXO. [4] [3].*

BabyIAXO has two 10-meter long bores that could collect axions and convert them into X-rays through a 2 Tesla lab magnetic field (Fig. 5). A larger cross sectional bore area increases the probability of collecting axions. BabyIAXO's bore area is close to $.77m^2$, which is 250 times bigger than the previous experiment CAST's cross sectional bore area [4]. The increased cross sectional bore area would allow BabyIAXO to collect more signals while also collecting more detector background, which would compromise sensitivity to the faint signals. To compensate, two optics will be implemented to focus the collected axion-converted X-ray signals from the two bores into smaller spots on detectors, giving a higher signal to noise ratio. BabyIAXO's goal is to focus the signal from a cross sectional bore area of $.77m^2$ to a spot size with diameter ~ 4 mm (spot size area $\approx 12mm^2$) [4]. Achieving a high signal to noise ratio requires a high-quality optic.

2 BabyIAXO X-ray Optic Design

The BabyIAXO X-ray optic shown in Fig. 6 is composed of concentric, tightly packed mirror shells divided into sextants, with inner and outer optics made using different

methods. X-rays are difficult to focus because they are high energy photons and tend to either get absorbed by a material or go straight through. In order to focus X-rays, you need both a shallow grazing angle (angle of incoming photon measured from the surface) and highly X-ray reflective material [10].

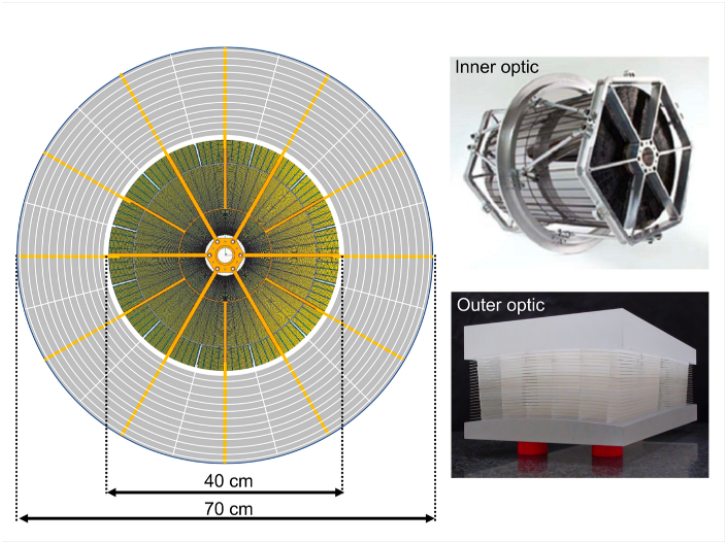

Figure 6: Left: *Top view of BabyIAXO geometry.* ***Top right:*** *Inner optic of Nuclear Spectroscopic Telescope Array (NuSTAR) that BabyIAXO's inner optic is based off of.* ***Bottom right:*** *"Cold slumped" glass technology for outer layers of optic [4].*

A telescope with shallow grazing angle can be accomplished using a specific X-ray focusing optical geometry known as the Wolter-I design (Fig. 7) [10].

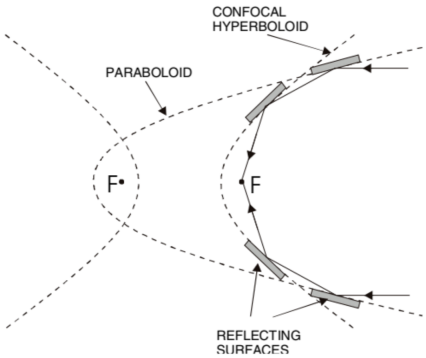

(a) *Wolter-I geometry for X-ray optic diagram. [10].*

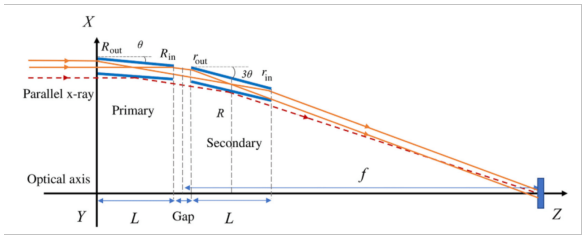

(b) *Side view of Wolter-I geometry with conical approximation [9].*

Figure 7: *Wolter-I X-ray optic geometry allows effective focusing of X-rays.*

The Wolter-I design involves a set of two mirrors: a paraboloid-shaped primary mirror and a hyperboloid-shaped secondary mirror. X-ray photons in this geometry bounce twice and focus on a common focal point shown in the middle of Fig. 7a. The primary mirror collects incoming X-rays, while the secondary mirror allows all the collected X-rays to focus at the same, shorter focal point [10]. This design allows X-ray focusing with a reasonable focal length. BabyIAXO's focal length was optimized to be 5 m [4]. Paraboloid and hyperboloid shaped mirrors are difficult and costly to manufacture in practice, so BabyIAXO uses a conical approximation of this Wolter-I geometry (Fig.

7b). Though this conical approximation introduces low systematic error, it is more cost effective with high quality results (e.g. hard X-ray telescope NuSTAR, which used a conical approximation of Wolter-I telescope, achieved an HPD (Sec. 3.2) of 58″ [5]).

To account for the decreased collecting area due to shallow grazing angle, BabyIAXO has 103 optical layers, or shells. The inner 50 shells make up the inner core optic, which will be created using thermal slumping technology. The inner core layers are split into sextants, each with a primary and secondary mirror. Each of the primary and secondary mirrors are also split in half due to the limited size of our thermal slumping furnaces (Sec. 3.1). This requires 1200 pieces of cylindrically shaped mirrors, each of which must meet the HPD goal of 60″ to focus the axion signals from the solar core onto the detectors with high signal-to-noise ratio.

3 X-ray Optic Fabrication Process

Cost effectively producing 1200 high quality mirrors on a reasonable timeline requires an organized and efficient optic fabrication process that can precisely control the figure error of the mirror, while taking stringent error budgets in every part of the production process to adapt as needed.

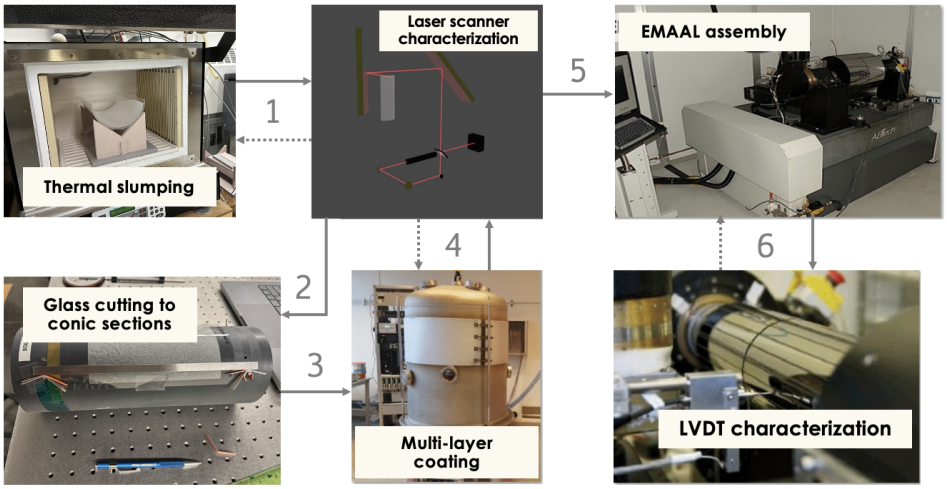

Figure 8: *Optic fabrication process diagram. Dotted arrows: indicate feedback from characterization methods. Solid arrows: indicate following step (image adapted from Kerstin Perez).*

The BabyIAXO X-ray optic fabrication process goes as follows:

1. Thermal slumping: Heat thin glass microsheets into a cylindrical shape using furnaces.

2. Laser scanner characterization: Characterize slumped glass sample qualities with a laser scanner.

3. Glass cutting to conical sections: Cut slumped glass samples into a specific trapezoidal shape based on glass' position in X-ray optic.

4. Laser scanner characterization: Characterize cut slumped glass samples with laser scanner.

5. Multi-layer coating: Send the cut slumped glasses to Technical University of Denmark (DTU) to coat with depth graded multi-layer coating to enhance X-ray reflectance, transforming glass samples into mirrors for the optic [4] [10]. Send glasses back to Columbia University.

6. Laser scanner characterization: Characterize coated glasses with laser scanner.

7. EMAAL assembly: Assemble X-ray optic in Nevis Labs cyclotron building clean room using EMAAL assembly machine, developed by NuSTAR [8].

8. LVDT characterization: Use linear variable differential transformer (LVDT) to characterize each step of the X-ray optic assembly. Use feedback to minimize overall error of X-ray optic.

This work aims to optimize the fabrication process until coating for 120 mm diameter slumped glass (BabyIAXO optic layers 6-8) to be repeated for other layers.

3.1 Thermal Slumping

The first step is to form the glass into a cylindrical shape. BabyIAXO utilizes thermally formed glass, which is a leading technology used to accommodate high surface quality and ultra-lightweight X-ray mirrors, to achieve high quality X-ray optics. Ney Vulcan 3-1750 furnaces (W 350 mm x H 270 mm x D 300 mm) are utilized to thermally slump borosilicate glass microsheets of type Schott D263 onto the concave side of semi-cylindrically shaped quartz mandrels, shown in Fig. 9a. Heating these glass microsheets decreases its viscosity, allowing the glass to anneal. This property is used to thermally form glass microsheets into the shape of the mandrels via gravity, the ideal process of which is shown in Fig. 9b.

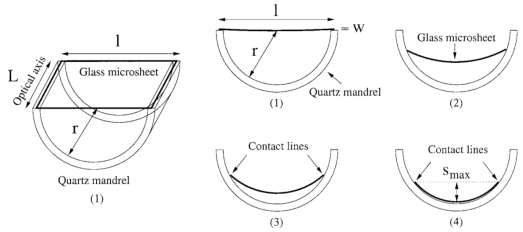

(a) *Side view of the thermal forming process. [7].*

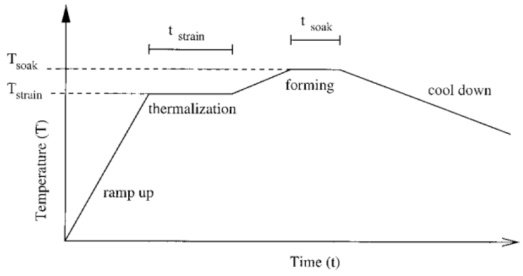

(b) *Graph of ideal process of thermal forming glass. Thermal forming of glass happens when the furnace temperature is around T_{soak} [7].*

Figure 9: *Thermal slumping process.*

Fig. 9b plots the temperature plotted against time to show the ideal process of thermally forming glass microsheets. The furnace temperature is increased at a rate of $15°C/min$ until the furnace temperature reaches $310°C$. The furnace temperature is then increased at a rate of $9°C/min$ until the furnace temperature reaches the strain point ($T_{strain} = 529°C$) and thermalizes for the strain time ($t_{strain} = 10min$). T_{strain} is the temperature at which glass behaves more like a liquid due to decreased viscosity and allows the glass to deform under the stress of gravity, while t_{strain} is the time required

for the glass to thermalize at this temperature. Finally, the glass is heated at a rate of $5°C/min$ until it reaches the soak temperature (T_{soak}), which is allowed to thermalize for the soak time (t_{soak}). Both the T_{soak} and t_{soak} differ depending on the sheet geometry based on the viscodynamic model for the thermal-forming process [7]. T_{soak} is higher than T_{strain} but lower than the glass' softening point ($\approx$ 600-700 $°C$). This ensures that the glass viscosity is low enough to mold to the mandrel's shape while staying high enough that the glass thickness doesn't change significantly during thermal forming [7].

Factors such as furnace temperature gradient, improper temperature probe calibration, convection in the furnace, impurities on the glass or mandrel surfaces, and the glass microsheet's placement on the mandrel can introduce figure errors in the slumped glass. Adjusting these parameters as well as the time and temperatures on the plot can help reduce these figure errors [7].

Mirror dimensions (l x w x d)	112 mm x [108-125 mm] x .2 mm
Number of mirrors	240
Smallest mirror radius	54 mm
Biggest mirror radius	62.5 mm
Mirrors per shell	12

Table 1: *Specifications for inner 10 layers of BabyIAXO optic.*

Table 1 shows the specifications for the inner 10 layers. The inner layers, which have the most curvature, are more susceptible to glass deformation, and therefore are the most difficult to create with high quality. This work will be part of inner core x-ray optics in the future.

3.2 Laser Scanner Characterization

Once the glass microsheets are cylindrically-shaped, the surface error must be precisely characterized to find the highest quality section of the glass.

The laser scanner setup (Fig. 10) uses movable linear and rotational stages to control the laser path and scan the full length and width of the glass. By centering the rotational mirror (right in Fig. 10) with the slumped glass' radius, the setup operates on the following idea: a laser shone from the center of a perfectly cylindrical mirror in any azimuthal direction reflects directly back, while a laser shone at points on an imperfect cylindrical mirror will be slightly deflected. Deflections indicate surface imperfections, allowing us to characterize the entire mirror via analyzing the reflected laser points.

In the distribution of reflected laser points, the diameter that encloses half the reflected points is called the Half Power Diameter (HPD). The HPD is the quantity we use to characterize the surface error on the slumped glass samples. The highest axion flux comes from the sun's core, so the BabyIAXO optic's HPD goal is $60''$ in order to roughly match the size of the sun's core [11].

The scanning procedure goes as follows:

1. Paint the back of the slumped glass samples with a thin coat of black paint mixture to absorb most of the laser light that would normally be reflected from the back surface of the glass. Allow the paint to dry on a flat surface ($\sim$ 1 hour).

2. A glass sample is manually aligned on the platform (blue arc at the top right of Fig. 10).

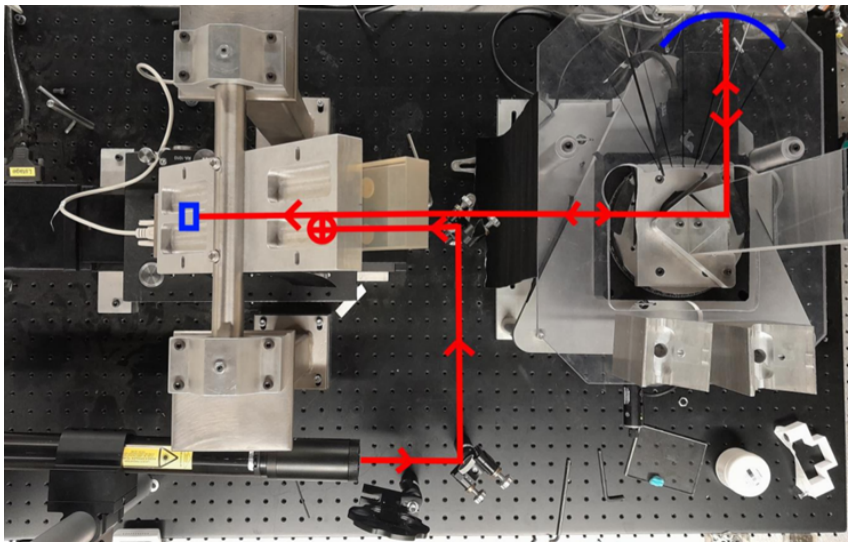

Figure 10: *Top view of laser scanner setup. The red line traces the laser path through the setup. The blue rectangle on the left indicates the detector's location, and the blue arc on the top right shows the slumped glass sample's location. Diagram by Mike Law.*

3. Use the LabView auto-alignment program to align the glass to higher precision.

4. The glass sample is scanned by the laser scanner system. The results are analyzed using the IDL program. The best 60° section from the 80° scan is documented.

Note: the black paint mixture is a 2:1 ratio of Sax Versatemp heavy-bodied tempera paint and fine ground sugar, which acts as a paint-thickening agent to adequately cover the back of the glass samples. Sugar is used over other paint thickeners because it has a similar index of refraction as our glass microsheets (~ 1.5). This allows the paint mixture to effectively absorb the second and greater order reflected laser light without creating further reflections off of the material interface created by the paint thickening agent.

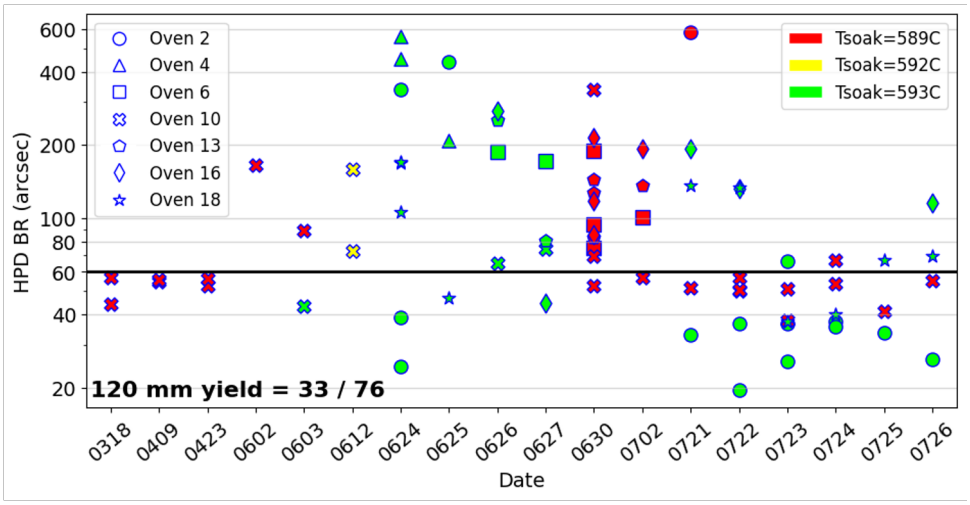

Figure 11: *HPD of glasses produced by 7 furnaces at different T_{soak} temperatures (Fig. 9b) plotted over time.*

Scanning provides valuable feedback for optimizing the slumping process. Figure 11 illustrates the HPD values obtained from each furnace over various days, with different

colors representing different temperature settings. Evidently, furnace 2 (circles at green temperature) and furnace 10 (x's at red temperature) consistently yielded glass samples with HPD values meeting our 60″ target. By using only the best-performing furnaces at their optimal temperatures, we significantly increased the production of glass samples with sufficient HPD and reduced those with poor HPD.

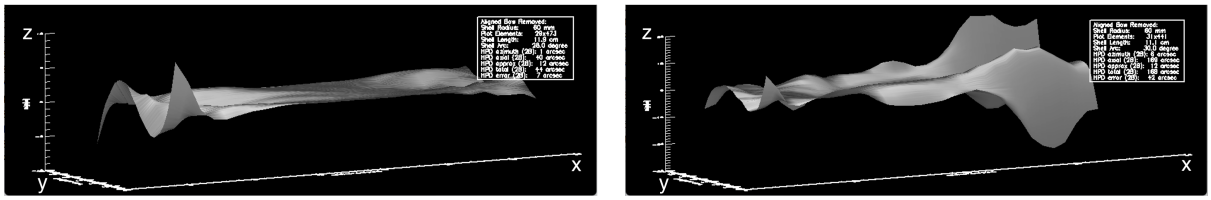

Figure 12: *Processed 3D surface profiles from IDL program. X-axis: Azimuthal position of scan (degrees). Y-axis: Axial position of scan (cm). Z-axis: surface error height (μm).* ***Left:*** *good quality glass, 44" HPD.* ***Right:*** *poor quality glass, 168" HPD, shows more variance. Note: scales are different between the two.*

Figure 12 shows the processed 3D profile scan from a scan of two slumped glass samples, flattened to display surface deviations from a perfect cylinder. Any deviations from the perfect cylinder negatively impacts the HPD, as we can see from the poor quality glass on the right.

3.3 Glass Cutting

The scanning results allow us to select which section of the glass samples with the lowest HPD to be cut and used in the BabyIAXO optic. BabyIAXO's inner optic will use sections that are 112 mm long and 60° wide for varying radii. In order to correctly fit the optic's conical shape, the glass samples must be cut into trapezoids.

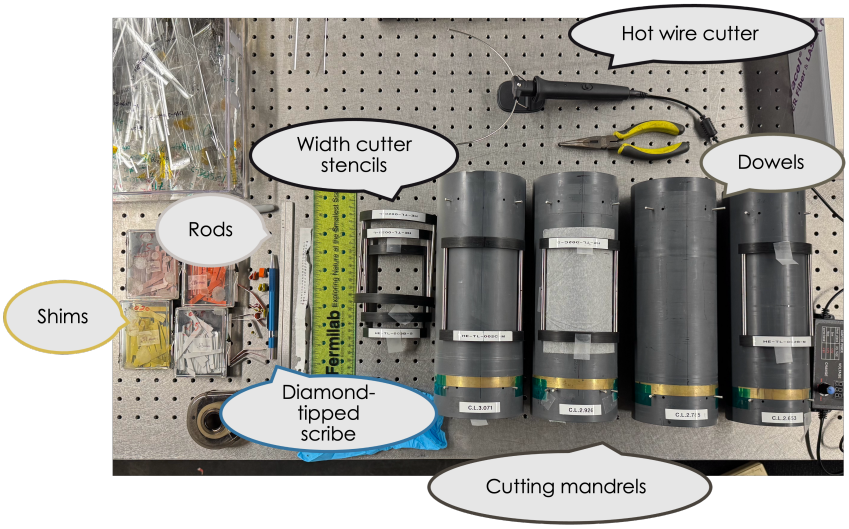

Figure 13: *Glass cutting setup. The items: Cutting mandrels of different sizes with dowels and matching width cutter stencils, rods of different sizes, shims of different sizes, a diamond-tipped scribe, and a hot wire cutter.*

The glass cutting procedure goes as follows (refer to Fig. 13 for a visual of the tools mentioned):

1. Place slumped glass sample on cutting mandrel.

2. Place rod on top of top and bottom dowels on cutting mandrel.

3. Score along rod. Apply gentle shear pressure to pinch either side of the crack to propagate crack along the scored line and "cut" the glass sample lengthwise. Repeat for the other side.

4. Place width cutter stencil on the glass sample resting on cutting mandrel.

5. Score along width cutter edge. Apply gentle shear pressure to pull either side of the crack to propagate crack along the scored line and "cut" the glass sample widthwise. Repeat for the second width cut.

Note from Fig. 6 that each optic layer has a unique radius, so each layer requires a unique grazing angle to maintain a shared focal point (Fig. 7b) [10]. This geometry requires different trapezoidal glass shapes for each layer. Therefore, the glass cutting process must be able to account for this.

Current cutting mandrels, designed for the High Energy Focusing Telescope (HEFT), cannot cut the specific trapezoidal geometry needed for BabyIAXO. Additionally, one diameter of slumped glass can cover multiple layers in the optic (e.g. 120 mm slumped glass can be cut into the appropriate shapes for layers 6-8 of the BabyIAXO optic), so each cutting mandrel needed to be adaptable to different modifications.

To achieve trapezoidal shapes, the cutting process needed to be modified by independently determining the top and bottom rod placements. This can be done by adding varying thicknesses of metal strips (shims) around the dowels. Using appropriately chosen modifications allows us to control the arc lengths of the cut glass samples based on the required optic mirror dimensions.

This became a geometry problem with practical considerations, such as accounting for the errors from stacking shims and rods and the buffer between the rod edge and where the diamond tipped scribe indents the glass. After finding and accounting for these practical considerations, the geometric solution was coded into a glass cutting spreadsheet, which serves as a tool for determining the appropriate shim and rod thicknesses, as well as the cutting location.

The glass cutting procedure with BabyIAXO-specific modifications goes as follows:

1. Find and mark the best location on glass to cut based on laser scanning data.

2. Using the glass cutting spreadsheet, determine correct rod and shim sizes to use based on the optic layer, section (primary/secondary), and placement (top/bottom).

3. Place correct rods and shims on cutting mandrel dowels. Score along the rod using the diamond tipped scribe.

4. Apply gentle shear pressure to pinch either side of the crack to propagate crack along the scored line and "cut" the glass sample lengthwise. Repeat for the other side.

5. Use the glass cutting spreadsheet to determine the where to place the width cutter, and score along the width. Repeat for the second width cut.

6. Bring a thin, hot wire (7 inch 32 AWG nichrome wire at 9V) close to the scored line and remove it. This allows the glass to slightly expand and contract, propagating a crack along the scored line and "cutting" the glass widthwise. Repeat for the second width cut.

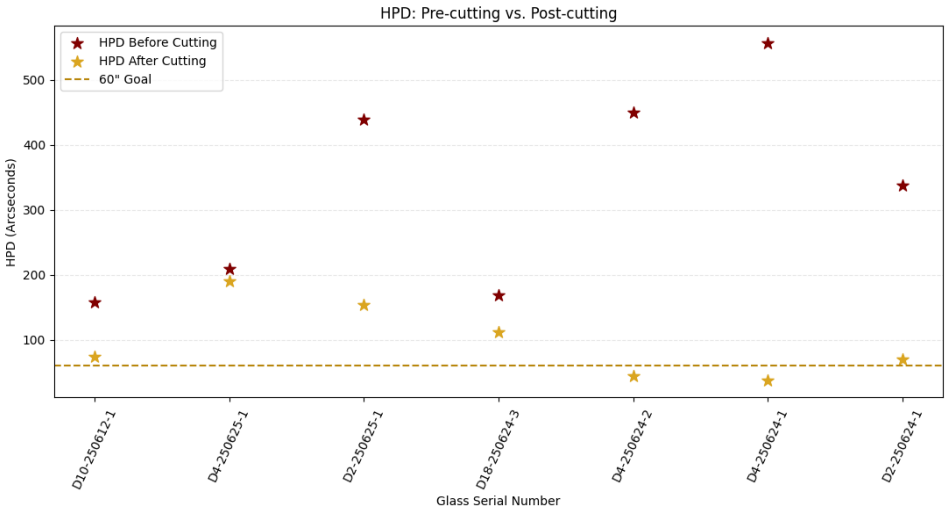

Figure 14: *HPD values, before and after cutting for 7 glass samples (serial numbers listed on x-axis).*

Cutting the glasses significantly improved their HPD, with reductions ranging from 9% to 90% across 7 samples that initially had poor HPDs (Fig. 14). This HPD improvement occurs because cutting weight off the sides of the glass releases tension, allowing the glass to flex outward into the correct radius. Fig. 14 shows the consistent improvement of poor quality glasses after cutting, some now meeting our HPD goal. The larger improvement (e.g. 557.0″ HPD to 37.8″ HPD) is likely due to poor overall glass shape error with minimal localized figure error, which can be corrected via cutting. The smaller improvement (e.g. 209.1″ HPD to 190.3″ HPD) is likely attributed to high localized figure error, which cannot be removed via cutting.

4 Future Work and Conclusions

In the end, we achieved our goal of mastering and streamlining the procedure for slumping, scanning, and cutting glass samples for layers 6-8 of the BabyIAXO X-ray optic.

We determined the optimal settings for slumping high quality cylindrical glass samples with 120 mm diameter, which correspond to the BabyIAXO layers 6-8. Through scanning 116 slumped glass samples and evaluating their qualities (Fig. 15), we refined our slumping process, significantly increasing the success rate of slumped glasses meeting our $60”$ HPD goal from under 30% to nearly 80%. We also established a precise cutting procedure, including methods for adjusting the cutting mandrel to accommodate varying glass geometries from different layers, and successfully implemented this process for producing all layers in the x-ray optic. Through practice and improved technique, we achieved a cutting yield of nearly 100%. Furthermore, we demonstrated that the cut-

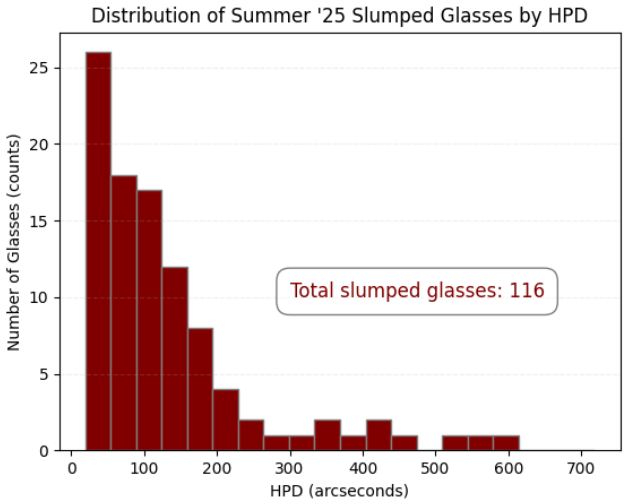

Figure 15: *Distribution of total number of glasses slumped this summer based on pre-cutting HPD values from scanning.*

ting process consistently enhances glass quality, eliminating the need for rescanning the glasses post-cutting.

This process of glass fabrication will be replicated for all BabyIAXO layers. The cut glass samples will be sent to DTU for coating and assembled into the optic in the cleanroom at Columbia's Nevis Labs. Our goal is to assemble the inner 10 layers of the BabyIAXO X-ray optic to take for calibration at the PANTER X-ray test facility by Spring 2026.

5 Acknowledgements

This material is based upon work supported by the National Science Foundation under Grant No. PHY-2349438. I'd like to acknowledge Prof. Kerstin Perez and the Perez Lab, the Nevis Labs REU led by Prof. Georgia Kariogiorgi and Prof. Reshmi Mukherjee, and the NSF Foundation, with a special thanks to my mentors Dr. Jooyun Woo and Dr. Yue Yu, and lab mate Efi.

References

[1] C. Abel, S. Afach, N. J. Ayres, C. A. Baker, G. Ban, and ... (et al.). Measurement of the Permanent Electric Dipole Moment of the Neutron. *Phys. Rev. Lett.*, 124(8):081803, 2020.

[2] Adams, C. B. and Aggarwal, N. and Agrawal, A. and Balafendiev, R. and Bartram, C. and ... (et al.). Snowmass 2021 White Paper: Axion Dark Matter. *arXiv*, 2203.14923(v3), 2023.

[3] E. Armengaud, D. Attie, S. Basso, P. Brun, N. Bykovskiy, and ... (et al.). Physics potential of the International Axion Observatory (IAXO). *arXiv*, 1904.09155(v3), 2019.

[4] The IAXO Collaboration. Conceptual design of babyiaxo, the intermediate stage towards the international axion observatory. *Journal of High Energy Physics*, 2021(5):137, May 2021.

[5] Fiona A. Harrison, William W. Craig, Paolo Giommi, and ... (et al.). The Nuclear Spectroscopic Telescope Array (NuSTAR) High-Energy X-ray Mission. Reprint 20140011114, NASA Technical Reports Server, 2013.

[6] Anson Hook. TASI Lectures on the Strong CP Problem and Axions. *arXiv*, 1812.02669(v3), 2023.

[7] Mario A. Jimenez-Garate, Charles J. Hailey, William W. Craig, and Finn E. Christen. Thermal forming of glass microsheets for x-ray telescope mirror segments. *Appl. Opt.*, 42(4):724–735, 2003.

[8] J. E. Koglin, H. An, K. L. Blaedel, N. F. Brejnholt, and ... (et al.). NuSTAR hard x-ray optics design and performance. In *Proceedings of SPIE - The International Society for Optical Engineering*, volume 7437, 2009.

[9] Yingyu Liao, Zhengxiang Shen, and Zhanshan Wang. Design of Conical Wolter-I Geometry with Sectioned Secondary Mirrors for X-Ray Telescopes. *Journal of Astronomical Telescopes, Instruments, and Systems*, 5(1):014004, January 2019.

[10] Richard Mushotzky. X-ray Telescopes. ASTR 480 course lecture notes, University of Maryland, 2000.

[11] Javier Redondo. Solar axion flux from the axion–electron coupling. *JCAP*, 12(008):008, 2013.

[12] P. Sikivie. Experimental Tests of the Invisible Axion. *Phys. Rev. Lett.*, 51:1415–1417, 1983.